ADVANCED MATERIALS

Supporting Information

Scalable Synthesis of Monolayer Hexagonal Boron Nitride on Graphene with Giant Bandgap Renormalization

Ping Wang, Woncheol Lee, Joseph P. Corbett, William H. Koll, Nguyen M. Vu, David Arto Laleyan, Qiannan Wen, Yuanpeng Wu, Ayush Pandey, Jiseok Gim, Ding Wang, Diana Y. Qiu, Robert Hovden, Mackillo Kira, John T. Heron, Jay A. Gupta,* Emmanouil Kioupakis,* and Zetian Mi*

Supporting Information

Scalable Synthesis of Monolayer Hexagonal Boron Nitride on Graphene with Giant Bandgap Renormalization

Ping Wang, Woncheol Lee, Joseph P. Corbett, William H. Koll, Nguyen M. Vu, David Arto Laleyan, Qiannan Wen, Yuanpeng Wu, Ayush Pandey, Jiseok Gim, Ding Wang, Diana Y. Qiu, Robert Hovden, Mackillo Kira, John T. Heron, Jay A. Gupta,* Emmanouil Kioupakis,* Zetian Mi*

Dr. P. Wang, W. Lee, Dr. D. A. Laleyan, Q. Wen, Dr. Y. Wu, Dr. A. Pandey, Dr. D. Wang, Prof. M. Kira, Prof. Z. Mi
Department of Electrical Engineering and Computer Science, University of Michigan,
Ann Arbor, MI 48109, USA
E-mail: ztmi@umich.edu
Dr. J. P. Corbett, W. H. Koll, J. A. Gupta
Department of Physics, Ohio State University,
Columbus, OH 43210, USA
E-mail: gupta.208@osu.edu
Dr. J. P. Corbett
UES, Inc., 4401 Dayton-Xenia Rd,
Dayton, Ohio 45432, USA
Dr. N. M. Vu, Dr. J. Gim, Prof. R. Hovden, Prof. J. T. Heron, Prof. E. Kioupakis
Department of Material Science and Engineering, University of Michigan,
Ann Arbor, MI 48109, USA
E-mail: kioup@umich.edu
Prof. D. Y. Qiu
Department of Mechanical Engineering and Materials Science, Yale University,
New Haven, CT 06516, USA

1. Energetic stability of hBN edges and hBN/G interfaces

Hexagonal boron nitride (hBN) has two types of atomic edges, including armchair (AC) edges with alternating B and N atoms (AC_{hBN}) and B-/N-terminated zigzag (ZZ) edges (ZZ_{B-hBN} and ZZ_{N-hBN}). Theoretical calculations suggested that their energetic stability are ranked in the order of $ZZ_{B-hBN} <$ $AC_{hBN} < ZZ_{N-hBN}$.[1] Therefore, triangular domains tend to terminate with ZZ_{N-hBN} edges, while hexagonal domains prefer to possess AC_{hBN} edges.[2-5] Both our experimental results and previous reports[6,7] show that hBN grown on graphene substrates consists of hexagonal or truncated hexagonal domains. Therefore, the growth front of hBN grown on graphene substrates prefer to terminate with AC_{hBN} edges, instead of ZZ_{hBN} edges, which has been also confirmed by transmission electron microscopy measurements for hBN grown on epitaxial graphene layers.[8]

Generally, during the growth on graphene substrates, hBN prefers to nucleate from the graphene atomic edges, leading to lateral epitaxy.[6,8] The AC and ZZ edges of graphene (G) and hBN enable the formation of a myriad of hBN/graphene (hBN/G) interfaces with different atomic configurations.[9-11] **Table S1** lists the most possible hBN/G interfaces predicted by theoretical calculations.[10,11] Clearly, the corresponding formation energy highly depends on the interface atomic configurations, in which $AC_G \| AC_{hBN}$ and $ZZ_G \| ZZ_{hBN}$ interfaces have relatively lower formation energy. Combining the hBN/G interface as well as the hBN growth front atomic configurations, we can predict that $AC_G \| AC_{hBN}$ interface-mediated growth leads to the formation of straight hBN nanoribbons, while an initiating $ZZ_G \| ZZ_{hBN}$ interface is expected to produce jagged hBN nanoribbons, as depicted in Figure 1a, b, respectively, in the main text.

Table S1. Formation energy (E_{form}) of in-plane hBN/G interfaces.[10,11]

	$AC_G \| AC_{hBN}$	$ZZ_G \| ZZ_{hBN}$	Misoriented
E_{form} (eV/nm)	2.2	2.8-2.9	≥4.4

2. Synthesis of monolayer hBN on HOPG

Figure S1 shows the typical morphologies of monolayer hBN grown on highly oriented pyrolytic graphite (HOPG) at growth temperature of 1000-1600 °C. In contrast to the monotypic atomic edges on single-crystalline metal substrates,[4] graphene substrates normally have mixture atomic edges, including both AC_G and ZZ_G edges. Therefore, shown in **Figure S2**, straight and jagged monolayer hBN nanoribbons co-exist on the HOPG surface. Additionally, due to the unintentionally formed surface damages during the HOPG fresh surface preparation, a few individual hBN domains were observed on top of graphene terrace. The individual domains have a clear hexagonal shape, while the nanoribbons consist of truncated hexagonal domains grown along the graphene atomic edges. However, the hexagonal domains that lead to formation of straight and jagged nanoribbons have different in-plane orientations, which were unequivocally confirmed by the orientation at the end of the nanoribbons, shown in Figure S1a, b. Based on above thermodynamic discussion, the straight and jagged morphologies suggest that the monolayer hBN nanoribbons grown along graphene atomic

edges initialized with different hBN/G interfaces. The graphene interface-mediated growth process is discussed in detail in the main text.

The density of nanoribbons dramatically decreased when growth temperature was increased to 1600 °C (Figure S1). However, the density of straight nanoribbons almost didn't change with growth temperature, while most of the jagged nanoribbons disappeared. The absence of jagged nanoribbons unambiguously evidences that the possibility of forming metastable $ZZ_G||ZZ_{hBN}$ interface is extremely suppressed at 1600 °C, which agrees well with the prediction of the interface-mediated growth model based on thermodynamics.

Figure S3a shows the low magnification scanning electron microscopy (SEM) image of the hBN nanoribbons grown at 1600 °C for 60 min. Shown in the insets are the zoom-in SEM images acquired from three representative areas, in which the width along the entire nanoribbons is very uniform. The small domain formed in the green box is due to the surface damage on HOPG. Shown in Figure S3b, topographic atomic force microscopy (AFM) image and the corresponding phase channel image confirmed that the individual nanoribbons are monolayer hBN with a thickness of ~0.35 nm.
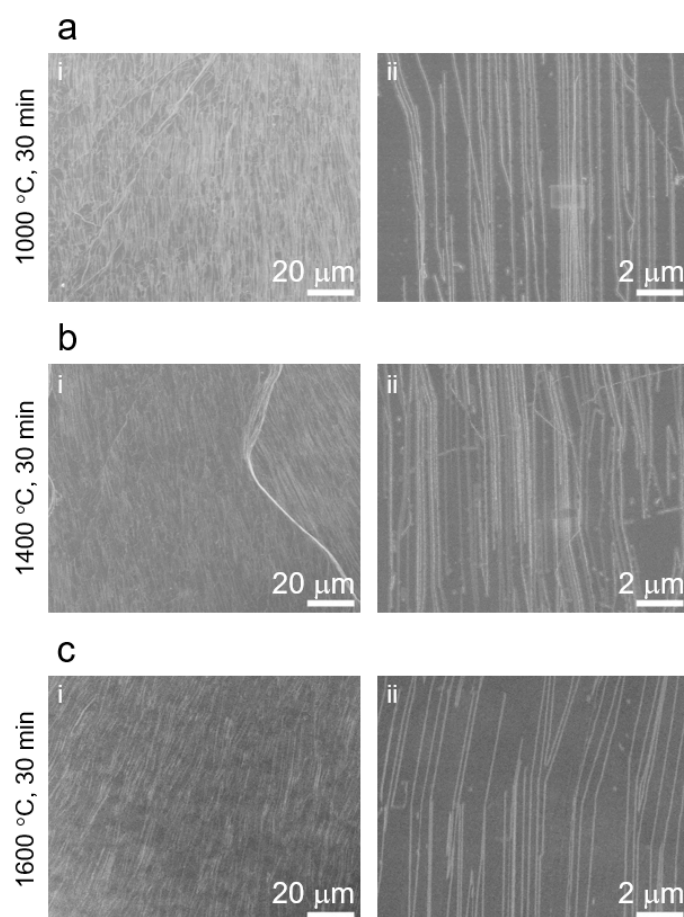

Figure S1. Surface morphology comparison of epitaxial monolayer hBN on HOPG with varying growth temperatures. a-c) hBN nanoribbons grown at a) 1000, b) 1400, and c) 1600 °C for 30 min. The nanoribbon density decreases dramatically as the growth temperature increases up to 1600 °C, and the straight nanoribbons dominate the growth.
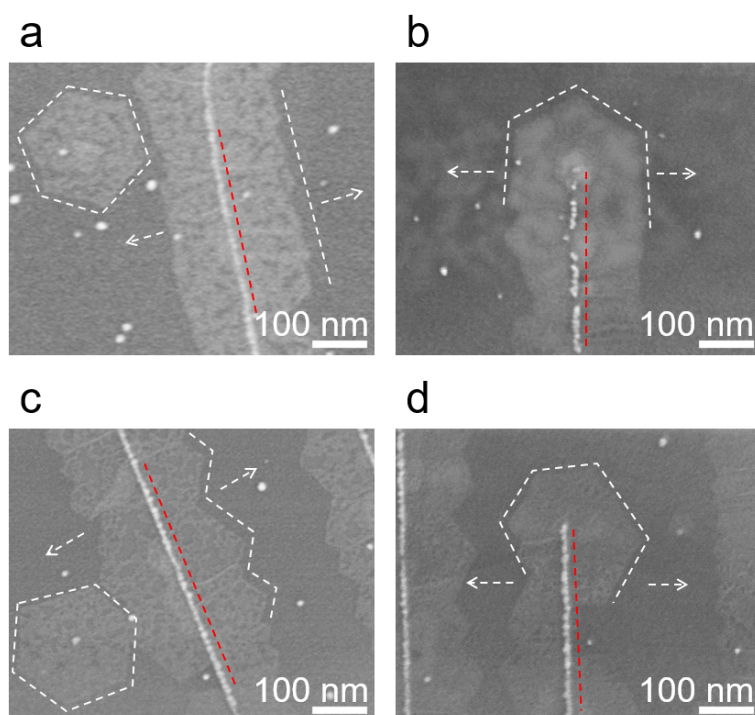
Figure S2. Typical morphologies of epitaxial monolayer hBN on HOPG. a) Straight monolayer hBN nanoribbon and b) the end of the straight nanoribbon. c) Jagged monolayer hBN nanoribbon and d) the end of the jagged nanoribbon. Red dashed and white dashed lines show the graphene atomic edges and outline of the growth fronts of monolayer hBN, respectively, and white dashed arrows indicate the growth direction. All the nanoribbons consist of truncated hexagonal domains, and the end of nanoribbons shows a clear hexagonal geometry. The individual hexagonal domains grown near the nanoribbons show the same orientation to the corresponding adjacent nanoribbons.
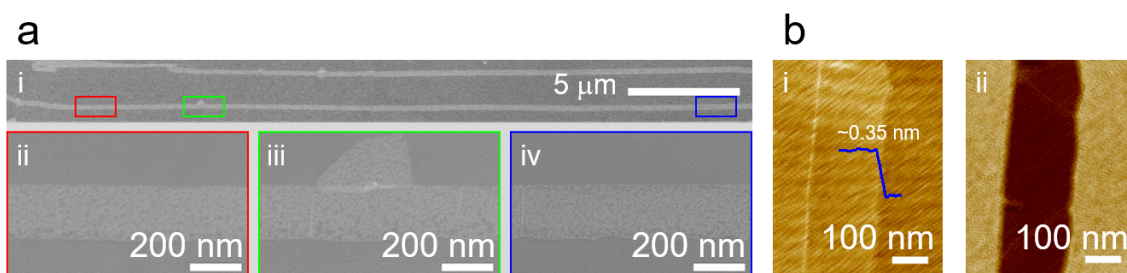

Figure S3. Uniformity of straight monolayer hBN nanoribbons. a) Low magnification SEM image of straight monolayer hBN nanoribbons grown at 1600 °C for 60 min. Insets are the high magnification SEM images captured from the red, green, and blue boxes, respectively. b) Height-channel (i) and phase-channel (ii) AFM images of a straight hBN nanoribbon, illustrating a thickness of ~0.35 nm for monolayer hBN.

3. Additional STM characterization of hBN nanoribbons: nanoribbon uniformity and growth front registry

Complementary to the SEM imaging, our large area STM images also show the straight hBN nanoribbons, such as the one to the left of **Figure S4**. A uniform moiré superlattice with single periodicity (~16 ± 1nm) is observed along the entire length imaged (~ 1 μm). Small strips of bilayer hBN are identified from analyzing step heights in this image, and do not show a moiré superlattice.

 Figure S5a shows an STM image acquired from a straight monolayer hBN nanoribbon growth front. Similar to the nucleation interface shown in the main text, the atomic termination is obscured by atomic-scale contrast likely due to defect states and/or edge contamination. However, the corresponding unit cell in real-space (red diamonds) and FFT (green diamonds) (Figure S5b, c) for the two regions exhibit hexagonal periodicities that are aligned between hBN and graphene. The same orientation of FFT indicates that the hBN shares the same orientation with the underlying graphene.
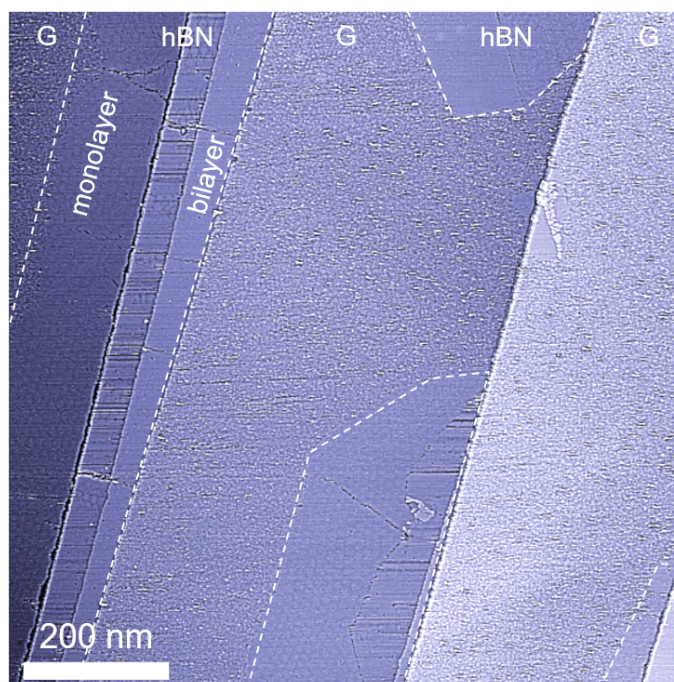

Figure S4. Large-area single periodicity moiré superlattice in epitaxial monolayer hBN on HOPG. Clear moiré superlattice with single periodicity is readily observed on monolayer hBN, while there is no clear moiré superlattice on bilayer hBN region.
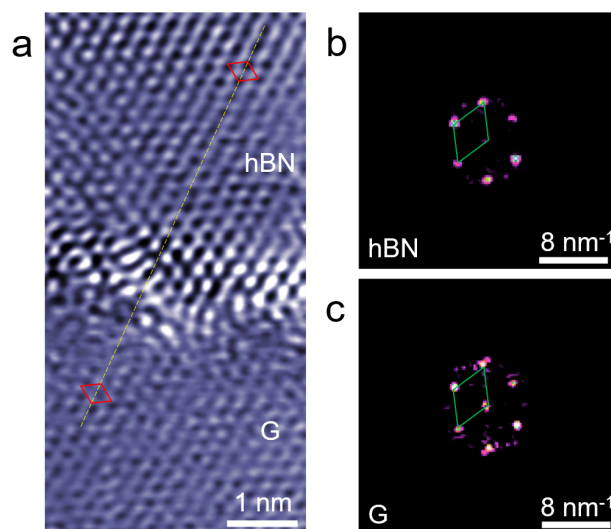
Figure S5. Atomic configuration of the growth front of epitaxial straight monolayer hBN nanoribbons on HOPG. a) STM image of a straight monolayer hBN nanoribbon growth front, b,c) the corresponding FFT of hBN and graphene regions, respectively. Red and green diamonds represent the corresponding unit cell in real- and reciprocal-space, respectively. Yellow-dashed line indicates the orientation of unit cells.

4. Electrical properties of epitaxial monolayer hBN on HOPG

Furthermore, the insulating properties and electrical reliability of the monolayer hBN were investigated using conductive atomic force microscopy (cAFM). A schematic of the cAFM measurement is presented in **Figure S6**a. Figure S6b shows the topographic AFM image of monolayer hBN grown on HOPG, the corresponding current map was acquired by applying a constant bias (0.01 V) between the HOPG substrate and cAFM tip (Figure S6c). The current map exhibits a distinct regional distribution of conductance, *i.e.*, the tunneling currents of hBN regions are significantly lower than that of uncovered HOPG regions. The outlines of uncovered HOPG were easily depicted from the current map as indicated by black dotted lines in Figure S6b. The bright sharp lines in the current map mainly result from the current fluctuation when doing contact-scan on HOPG substrate.[12]

The height and current profiles recorded along the white arrows labeled in Figure S6b-d are plotted in Figure S6e. This investigated region is highlighted in Figure S6d (bottom panel). It is clear that the abrupt current change is independent of morphology and only appears at the hBN/G interfaces, suggesting the current map was highly tailored by hBN. In the current profile of hBN, we observe a narrow region with no obvious fluctuation, as highlighted in the inset of current profile, which corresponds to another monolayer step in the height profile. A narrow ribbon area with monothetic color is also observed in the current map (enclosed by white dotted lines in Figure S6c), indicating the existence of a bilayer hBN region, consistent with the observations in SEM images (Figure 1g). As shown in the atomic schematic of Figure S6d (top panel), the doubled tunneling barrier thickness in a vertical vdW stacking configuration results in the decrease of tunneling current under the same bias.[13]

Furthermore, electrical breakdown tests have been executed on the hBN nanoribbons grown at 1600 °C. **Figure S7**a, b show the topographic image and the corresponding current map of hBN/HOPG. Localized *I-V* measurements (*i.e.*, breakdown tests) were performed on different spots. Figure S7c presents two representative *I-V* curves recorded from two points labeled as #1 and #2 in Figure S7b. Exponential fitting was carried out to illustrate the envelope of the suddenly increased current. The randomly fluctuated current after breakdown is due to the incomplete formation of conduction path, which stabilizes with increasing bias[14]. The breakdown voltage was deduced from the intersection of the linear fitting of initial direct tunneling region and the exponential increasing region (black dashed lines). The acquired breakdown voltages for hBN from point #1 and #2 are 0.29 and 0.42 V, respectively. Considering the thickness of monolayer hBN measured in this work is ~0.35 nm, a breakdown field range of 8-12 MV/cm has been achieved for the epitaxial hBN on HOPG, suggesting these unique hBN nanoribbons are promising insulating layer for the fabrication of 2D vdW devices. The recorded breakdown fields are located in the range of previously reported breakdown strength for hBN[13-15], while the variation may due to the surface defects which form during high-temperature growth and the nonuniform fluctuation of HOPG morphology.[16]
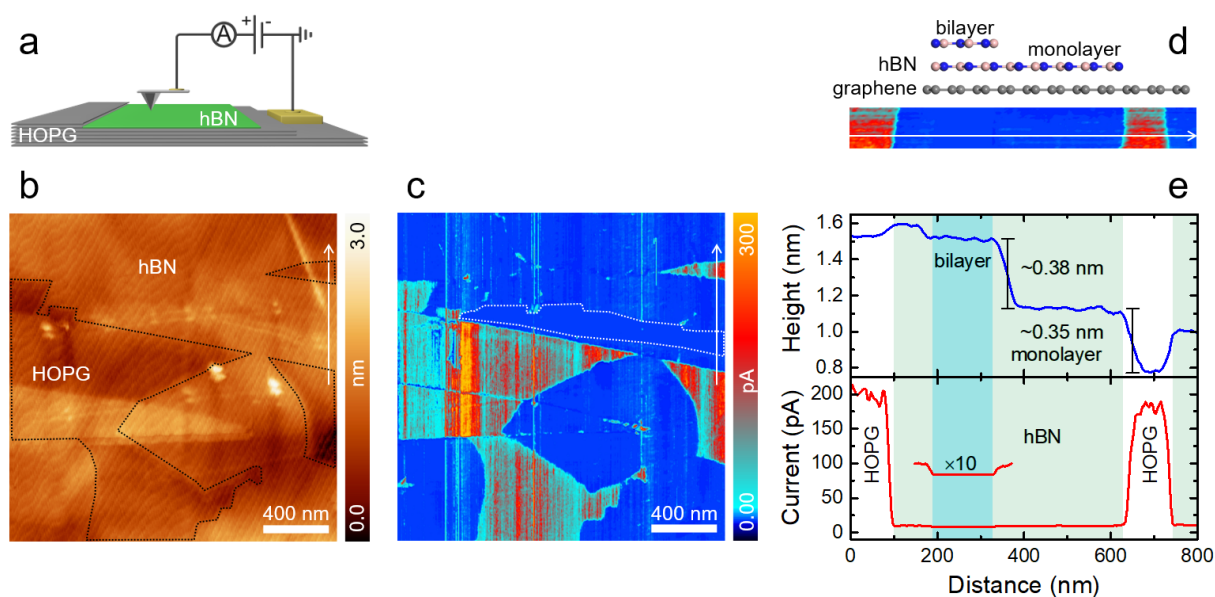

Figure S6. Electrical properties of epitaxial monolayer hBN on HOPG. a) Schematic of cAFM measurement. b) Topographic AFM image and c) corresponding current map of hBN grown on HOPG. Black-dotted lines in (b) depict the outlines of uncovered HOPG. White dotted lines in (c) indicate a bilayer hBN region. d) Magnification of the current map where uncovered HOPG, monolayer hBN, and bilayer hBN coexist (bottom), and the corresponding atomic model (top). e) Height (top) and current (bottom) profiles recorded along the white arrow in (b-d).
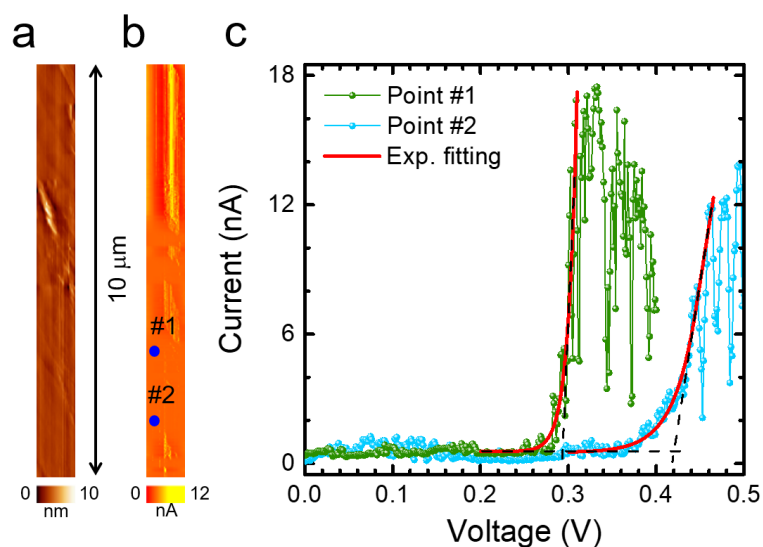
Figure S7. Breakdown test of epitaxial monolayer hBN on HOPG. a) Topographic AFM image and b) corresponding current map of hBN grown at 1600 °C for 120 min. c) Two representative *I-V* curves recorded from spot #1 and #2 labeled in b).

5. Optical emission of epitaxial monolayer hBN on HOPG

Figure S8a shows the photoluminescence (PL) spectrum of hBN/HOPG grown at 1600 °C. For comparison, PL spectra and corresponding reflectance spectra of hBN/HOPG grown at 800 and 1000 °C were collected at room-temperature (300 K). There are also a lot monolayer hBN on the surface of these two samples but with poor uniformity, and high density of multilayer hBN or hBN nanoparticles. Shown in Figure S8b, the dip positions in the reflectance spectra of hBN grown at 800 and 1000 °C are also at ~ 6.12 eV, suggesting a strong light-matter coupling with the presence of monolayer hBN. Accordingly, hBN/HOPG grown at 800 °C exhibits a small shoulder at ~ 6.12 eV, with a dominant broad peak at 5.75 eV and a wide sideband below 5.6 eV in the PL spectrum. However, the hBN/HOPG grown at 1000 °C presents a broad shoulder at ~ 6.12 eV, with a prominent broad peak at 5.75 eV. The asymmetric broadening of the sideband peak below 5.6 eV can be attributed to defects emission.[17,18] Compared with the PL spectrum acquired from the hBN grown at 1600 °C (Figure 3b in the main text), the PL spectra shown in Figure S8a are dominated by the contributions from multilayer hBN and defects, while the emission from monolayer hBN is also observable but has a weak intensity. Figure S8c presents the temperature-dependent PL spectra measured on the epitaxial hBN on HOPG (sample of Figure 1g). The triplet feature is well maintained up to 300 K. A large internal quantum efficiency ~40% was estimated for the highest emission peak (6.12 eV), suggesting monolayer hBN is a promising candidate for high performance deep-ultraviolet (UV) optoelectronic applications.
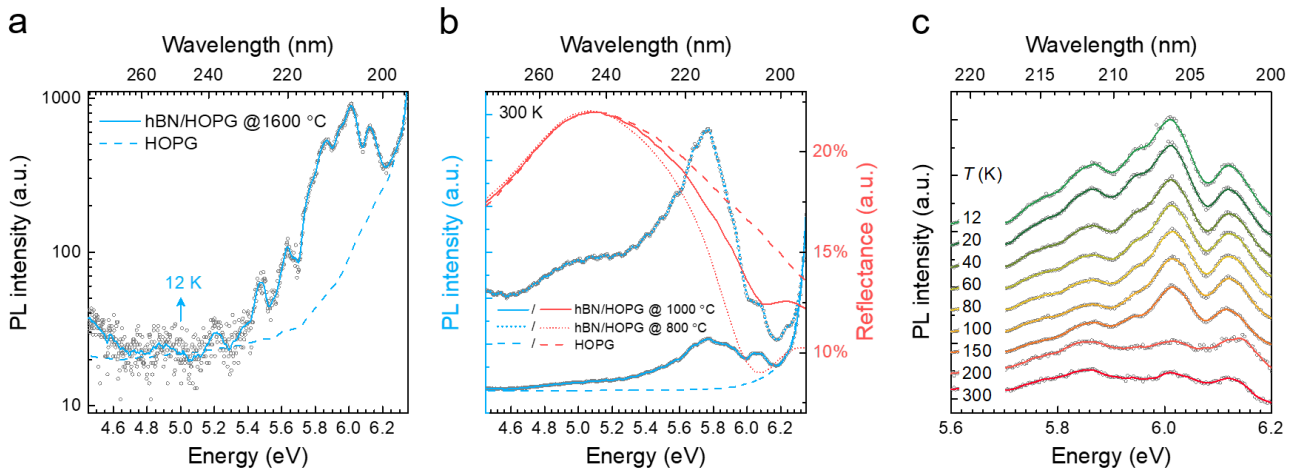
Figure S8. Deep-UV emission of epitaxial hBN on HOPG. a) PL spectrum of hBN/HOPG heterostructure grown at 1600 °C (logarithmic scale of Figure 3b, 12 K). b) PL spectra (blue curves) and reflectance spectra (red curves) of the hBN/HOPG heterostructures grown at 800 (dotted curves) and 1000 °C (solid curves), and HOPG substrate (dashed curves) (300 K). c) Temperature-dependent PL spectra of hBN grown at 1600 °C for 90 min on HOPG (after subtraction of stray laser light, spectra are shifted vertically for clarity). The gray circles are the PL data for hBN/HOPG heterostructures, while the blue solid curve in (a), blue solid curve and blue dotted curve in (b), and solid curves in (c) are the smoothed PL spectra.

6. *Ab initio* calculations of the band structure for monolayer hBN on graphene

We studied the electronic and optical properties of a monolayer hBN using first-principles calculations based on density functional theory (DFT) and many-body perturbation theory. It is known that hBN and graphene have very similar lattice constant ($a_{hBN} = 2.504$ Å[19] and $a_G = 2.464$ Å[20]). In this work, we used the in-plane lattice parameter of graphene for both supercell calculations to directly compare the screening effect from each material. Also, we assumed a ~40 Å thickness of vacuum layer to prevent the interaction between periodic images. Furthermore, we considered three different stacking configurations for the monolayer hBN/G interface (AA' stacking, Boron-centered AB stacking, and Nitrogen-centered AB stacking), as shown in **Figure S9**. We set the distance between monolayer hBN and graphene layers as $d = 3.5$ Å based on the AFM measurement results. This experimental value matches with the previously reported value.[18]

Based on these supercell structures, DFT calculations were performed within the Quantum Espresso code.[21] We used norm-conserving pseudopotentials and the local density approximation (LDA) for the exchange-correlation functional.[22,23] Electronic band structure calculations were performed on $18 \times 18 \times 1$ Monkhorst-Pack mesh. A plane cutoff energy of 70 Ry converged the total energy to within 1mRy/atom.

Next, the quasiparticle energy is obtained from the G_0W_0 method, as implemented in the BerkeleyGW code.[24] We used the screening cutoff energy of 30 Ry and included 1100 bands for the quasiparticle calculation. We adopted the generalized plasmon-pole model for the calculation of frequency-dependent dielectric effects[25] and the static-remainder approach to increase the computation speed and achieve the better convergence of the self-energy corrections.[26] Also, a

Wigner-Seitz slab truncation is employed to eliminate the artificial interaction between periodic images[27]. Furthermore, we applied nonuniform neck subsampling method to effectively treat the complicated screening of two-dimensional (2D) materials caused by the out-of-plane local fields and achieve better Brillouin zone sampling.[27] Using the GW-corrected quasiparticle energies, we interpolated the band structure on finer grids using the Maximally-localized Wannier function method[28] with Wannier90 code.[29]

Due to the complexity and the heavy computation cost of optical calculations for the metal–semiconductor heterostructure, we took the screening of the graphene into account using the substrate-screening method, *i.e.* by treating the substrate as a dielectric medium but without explicitly including its electrons into the quantum-mechanical calculations.[30] First, we built two different supercells, one containing the monolayer hBN and the other containing one to three graphene layers (nG, $n = 1, 2, 3$). Next, we calculated the irreducible polarizability matrix of monolayer hBN $\chi_{\mathbf{GG'}}^{0,\text{hBN}}$ and graphene $\chi_{\mathbf{GG'}}^{0,\text{G}}$ using the BerkeleyGW code.[24] In order to include the screening effect from the graphene, we set a total polarizability matrix $\chi_{\mathbf{GG'}}^{0,\text{total}} = \chi_{\mathbf{GG'}}^{0,\text{hBN}} + \chi_{\mathbf{GG'}}^{0,\text{G}}$ and calculate the dielectric matrix as $\tilde{\epsilon}_{\mathbf{GG'}}^{-1}(\mathbf{q}) = \left[1 - v\chi^{0,\text{total}}(\mathbf{q})\right]_{\mathbf{GG'}}^{-1}$. Especially, it is known that the dielectric function of graphene depends linearly on the density of states in case of the long-wavelength limit ($q \to 0$).[31] So we adopted a $160 \times 160 \times 1$ dense Monkhorst-Pack mesh for the $q \to 0$ limit to precisely capture the screening effect of the graphene layers. We used the dielectric matrix and the quasiparticle band structure obtained from this substrate-screening method for the following calculations. **Figure S10** shows the quasiparticle band structure of monolayer hBN sitting on one to three graphene layers (hBN/nG, $n = 1, 2, 3$), showing a giant bandgap renormalization. Details are discussed in the main text.

Finally, we solved Bethe-Salpeter equation to obtain the excitonic properties.[32] We interpolated the Coulomb matrix elements calculated on a coarse $18 \times 18 \times 1$ k-grid into a finer $80 \times 80 \times 1$ k-grid using the dual-grid method. The top two valence bands and the bottom two conduction bands of monolayer hBN were included in the calculation. The convergence of the exciton energy with respect to the fine $N_k \times N_k \times 1$ k-grid is shown in **Figure S11**.

Furthermore, to get a better understanding on the substrate-screening effect, we visualized the $1s$-exciton state by plotting the $1s$-exciton wavefunction,

$$\Psi(\mathbf{r}_e, \mathbf{r}_h) = \sum_{\mathbf{k},c,v} A_{vc\mathbf{k}}^S \psi_{c\mathbf{k}}(\mathbf{r}_e)\psi_{v\mathbf{k}}(\mathbf{r}_h), \qquad (1)$$

where $A_{vc\mathbf{k}}^S$ is an electron-hole amplitude, and $\mathbf{r}_e$ and $\mathbf{r}_h$ are the position of an electron and a hole, respectively. We fix the position of the hole (red dot in Figure 3d of the main text) to be slightly below the nitrogen atom of monolayer hBN layer and plotted the corresponding electron distribution. The isosurface level is set to be 3% of the maximum isovalue. The probability of finding the electron is maximum for the nearest boron atoms and the in-plane distribution shows the character of *sp2* orbitals. We also focused on the wavefunction distribution along the out-of-plane direction (*c*-axis). We find that most of the charge is confined within the monolayer hBN region, showing 2D-like

exciton wavefunction. This indicates that the graphene layers that are located further away than the adjacent layers do not have a significant effect on the monolayer hBN layer. Also, it has been previously reported that there is no noticeable difference between the screening effect from bilayer graphene and a HOPG substrate for $MoSe_2$ monolayer.[33] Therefore, we conclude that including only a few layers of graphene from the HOPG substrate for simulation reflects the actual substrate-screening effect on the exciton energies and wavefunctions.
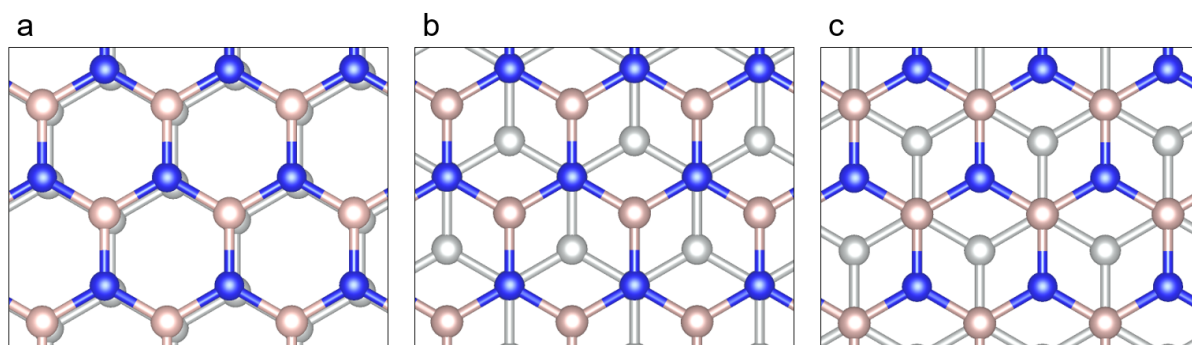

Figure S9. Staking configurations for the vertical hBN/G interface. a) AA' stacking, b) boron-centered AB stacking, and c) nitrogen-centered AB stacking configurations between monolayer hBN and graphene layer. Brown, blue, and gray balls indicate B, N, and C atoms respectively.
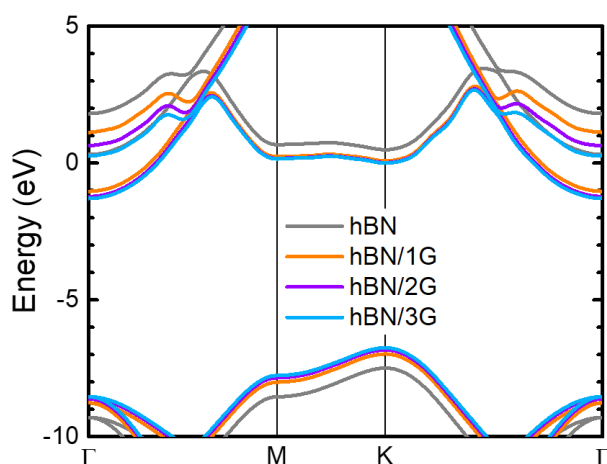

Figure S10. Quasiparticle band structure of freestanding monolayer hBN and monolayer hBN on one to three graphene layers.
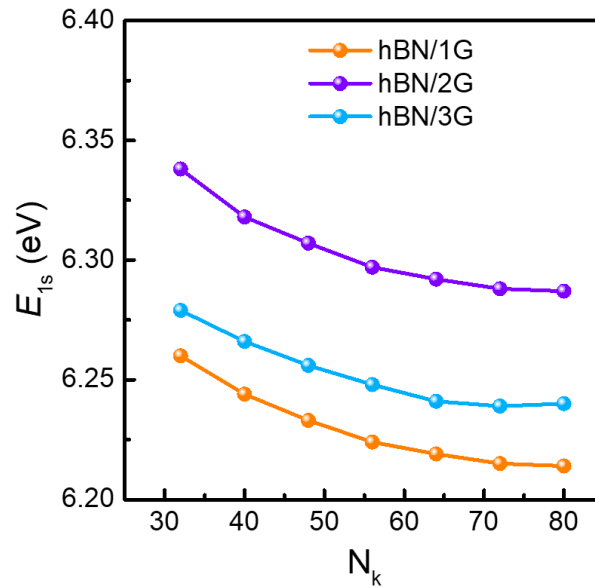
Figure S11. Convergence of the 1*s*-exciton energy of the monolayer hBN with varying number of graphene layers with respect to the number of *k*-points of the fine grid. $80 \times 80 \times 1$ fine *k*-grid converged the exciton energy within 5 meV.

7. Substrate-screening method

In **Table S2**, we summarized the direct gap of monolayer hBN on graphene obtained from G_0W_0 with explicit calculations including substrate electrons $\left(E_g^{G_0W_0}\right)$ and G_0W_0 with the substrate-screening method $\left(E_g^{G_0W_0,\text{Sub}}\right)$ that treats the substrate only as a dielectric medium. To analyze the origin of the small discrepancy between the two methods, we compared the RPA dielectric matrix elements obtained with and without using the substrate-screening method. Shown in **Figure S12**, we plotted the inverse of the head of the inverse dielectric matrix, $1/\varepsilon^{-1}_{\mathbf{G}=0,\mathbf{G}'=0}$, which contributes to the long-range screening effect. We confirmed that the matrix components obtained from two different methods are almost the same, with the error being less than 1%. This result demonstrates that the interlayer hybridization between monolayer hBN and graphene is negligible due to their weak vdW interactions, and the separate treatment of the screening from monolayer hBN and graphene can precisely capture the total screening of the system.

We attribute the difference between the two methods to the different total charge used in the plasmon-pole approximation (PPA). Since PPA takes the charge density for *f*-sum rule, a different total charge is used in the substrate-screening method $(\rho_{\text{total}} = \rho_{\text{hBN}})$ and the explicit substrate calculation $(\rho_{\text{total}} = \rho_{\text{hBN}} + \rho_{\text{G}})$. This difference results in slightly different quasiparticle energies. However, we confirm that the band structure obtained from the substrate-screening method fits well with the band structure obtained from the explicit substrate calculation when a small constant shift $\Delta E \left(= E_g^{G_0W_0} - E_g^{G_0W_0,\text{Sub}}\right)$ is applied. Therefore, we conclude that the difference in the bandgap value is not from dielectric calculations, but mainly from the plasmon-pole approximation used in

quasiparticle calculations. In subsequent BSE calculations, we used the band structure from the substrate-screening method with a constant shift $\left(\Delta E_g = E_g^{G_0W_0} - E_g^{G_0W_0,Sub}\right)$ applied to obtain accurate optical properties of monolayer hBN while reducing the computation cost.

Table S2. Quasiparticle bandgap of monolayer hBN with varying number of graphene layers obtained from G_0W_0 with explicit substrate calculation $\left(E_g^{G_0W_0}\right)$ and G_0W_0 with the substrate-screening method $\left(E_g^{G_0W_0,Sub}\right)$. Boron-centered AB stacking configuration is assumed for the vertical hBN/G interface.

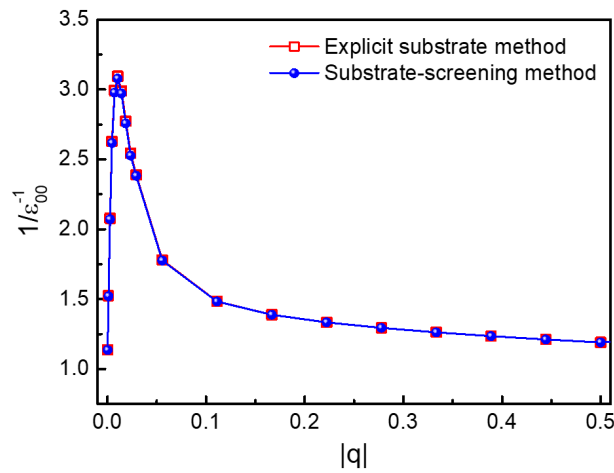|	$E_g^{G_0W_0,Normal}$	$E_g^{G_0W_0,Sub}$	ΔE_g
hBN/1G	7.11 eV	7.07 eV	0.04 eV
hBN/2G	6.98 eV	6.82 eV	0.16 eV
hBN/3G	6.95 eV	6.68 eV	0.27 eV

Figure S12. Inverse of the head of the inverse dielectric matrix values $\left(1/\varepsilon_{G=0,G'=0}^{-1}\right)$ of monolayer hBN on three graphene layers heterostructure obtained with and without the substrate-screening method. Boron-centered AB stacking configuration is assumed for the vertical monolayer hBN/G interface.

References:

[1] X. Fu, R. Zhang, *Nanoscale* **2017**, *9*, 6734.

[2] J. S. Lee, S. H. Choi, S. J. Yun, Y. I. Kim, S. Boandoh, J.-H. Park, B. G. Shin, H. Ko, S. H. Lee, Y.-M. Kim, *Science* **2018**, *362*, 817.

[3] X. Chen, H. Yang, B. Wu, L. Wang, Q. Fu, Y. Liu, *Adv. Mater.* **2019**, *31*, 1805582.

[4] L. Wang, X. Xu, L. Zhang, R. Qiao, M. Wu, Z. Wang, S. Zhang, J. Liang, Z. Zhang, Z. Zhang, *Nature* **2019**, *570*, 91.

[5] T.-A. Chen, C.-P. Chuu, C.-C. Tseng, C.-K. Wen, H.-S. P. Wong, S. Pan, R. Li, T.-A. Chao, W.-C. Chueh, Y. Zhang, *Nature* **2020**, *579*, 219.

[6] Y.-J. Cho, A. Summerfield, A. Davies, T. S. Cheng, E. F. Smith, C. J. Mellor, A. N. Khlobystov, C. T. Foxon, L. Eaves, P. H. Beton, S. V. Novikov, *Sci. Rep.* **2016**, *6*, 34474.

[7] J. Wrigley, J. Bradford, T. James, T. S. Cheng, J. Thomas, C. J. Mellor, A. N. Khlobystov, L. Eaves, C. T. Foxon, S. V. Novikov, *2D Mater.* **2021**, *8*, 034001.

[8] D. J. Pennachio, C. C. Ornelas-Skarin, N. S. Wilson, S. G. Rosenberg, K. M. Daniels, R. L. Myers-Ward, D. K. Gaskill, C. R. Eddy Jr, C. J. Palmstrøm, *J. Vac. Sci. Technol. A: Vac. Surf. Films* **2019**, *37*, 051503.

[9] Y. Liu, S. Bhowmick, B. I. Yakobson, *Nano Lett.* **2011**, *11*, 3113.

[10] S. Bhowmick, A. K. Singh, B. I. Yakobson, *J. Phys. Chem. C* **2011**, *115*, 9889.

[11] J. Zhang, W. Xie, X. Xu, S. Zhang, J. Zhao, *Chem. Mater.* **2016**, *28*, 5022.

[12] A. Summerfield, A. Kozikov, T. S. Cheng, A. Davies, Y.-J. Cho, A. N. Khlobystov, C. J. Mellor, C. T. Foxon, K. Watanabe, T. Taniguchi, *Nano Lett.* **2018**, *18*, 4241.

[13] L. Britnell, R. V. Gorbachev, R. Jalil, B. D. Belle, F. Schedin, M. I. Katsnelson, L. Eaves, S. V. Morozov, A. S. Mayorov, N. M. Peres, *Nano Lett.* **2012**, *12*, 1707.

[14] Y. Hattori, T. Taniguchi, K. Watanabe, K. Nagashio, *ACS Nano* **2015**, *9*, 916.

[15] G.-H. Lee, Y.-J. Yu, C. Lee, C. Dean, K. L. Shepard, P. Kim, J. Hone, *Appl. Phys. Lett.* **2011**, *99*, 243114.

[16] R. J. P. Román, F. J. Costa, A. Zobelli, C. Elias, P. Valvin, G. Cassabois, B. Gil, A. Summerfield, T. S. Cheng, C. J. Mellor, *2D Mater.* **2021**, *8*, 044001.

[17] D. A. Laleyan, K. Mengle, S. Zhao, Y. Wang, E. Kioupakis, Z. Mi, *Opt. Express* **2018**, *26*, 23031.

[18] C. Elias, P. Valvin, T. Pelini, A. Summerfield, C. Mellor, T. Cheng, L. Eaves, C. Foxon, P. Beton, S. Novikov, *Nat. Commun.* **2019**, *10*, 2639.

[19] R. S. Pease, *Acta Crystallographica* **1952**, *5*, 356.

[20] P. Trucano, R. Chen, *Nature* **1975**, *258*, 136.

[21] P. Giannozzi, O. Andreussi, T. Brumme, O. Bunau, M. B. Nardelli, M. Calandra, R. Car, C. Cavazzoni, D. Ceresoli, M. Cococcioni, N. Colonna, I. Carnimeo, A. D. Corso, S. d. Gironcoli, P. Delugas, R. A. DiStasio, A. Ferretti, A. Floris, G. Fratesi, G. Fugallo, R. Gebauer, U. Gerstmann, F. Giustino, T. Gorni, J. Jia, M. Kawamura, H.-Y. Ko, A. Kokalj, E. Küçükbenli, M. Lazzeri, M. Marsili, N. Marzari, F. Mauri, N. L. Nguyen, H.-V. Nguyen, A. Otero-de-la-Roza, L. Paulatto, S. Poncé, D. Rocca, R. Sabatini, B. Santra, M. Schlipf, A. P. Seitsonen, A. Smogunov, I. Timrov, T. Thonhauser, P. Umari, N. Vast, X. Wu, S. Baroni, *J. Phys.-Condens. Mat.* **2017**, *29*, 465901.

[22] D. M. Ceperley, B. J. Alder, *Phys. Rev. Lett.* **1980**, *45*, 566.

[23] J. P. Perdew, A. Zunger, *Phys. Rev. B* **1981**, *23*, 5048.

[24] J. Deslippe, G. Samsonidze, D. A. Strubbe, M. Jain, M. L. Cohen, S. G. Louie, *Computer Physics Communications*

2012, *183*, 1269.

[25] M. S. Hybertsen, S. G. Louie, *Phys. Rev. B* **1986**, *34*, 5390.

[26] J. Deslippe, G. Samsonidze, M. Jain, M. L. Cohen, S. G. Louie, *Phys. Rev. B* **2013**, *87*, 165124.

[27] H. Felipe, D. Y. Qiu, S. G. Louie, *Phys. Rev. B* **2017**, *95*, 035109.

[28] N. Marzari, A. A. Mostofi, J. R. Yates, I. Souza, D. Vanderbilt, *Rev. Mod. Phys.* **2012**, *84*, 1419.

[29] G. Pizzi, V. Vitale, R. Arita, S. Blügel, F. Freimuth, G. Géranton, M. Gibertini, D. Gresch, C. Johnson, T. Koretsune, *J. Phys.-Condens. Mat.* **2020**, *32*, 165902.

[30] M. M. Ugeda, A. J. Bradley, S.-F. Shi, H. Felipe, Y. Zhang, D. Y. Qiu, W. Ruan, S.-K. Mo, Z. Hussain, Z.-X. Shen, *Nat. Mater.* **2014**, *13*, 1091.

[31] E. Hwang, S. D. Sarma, *Phys. Rev. B* **2007**, *75*, 205418.

[32] M. Rohlfing, S. G. Louie, *Phys. Rev. B* **2000**, *62*, 4927.

[33] Y. Wang, S. Zhang, D. Huang, J. Cheng, Y. Li, S. Wu, *2D Mater.* **2016**, *4*, 015021.